



Testing the near-field Gaussian plume inversion flux quantification technique using unmanned aerial vehicle sampling

Adil Shah¹, Joseph R. Pitt¹, Hugo Ricketts^{1,2}, J. Brian Leen³, Paul I. Williams^{1,2},
Khristopher Kabbabe⁴, Martin W. Gallagher¹, Grant Allen¹

5 ¹Centre for Atmospheric Science, The University of Manchester, Oxford Road, Manchester, M13 9PL, United Kingdom

²National Centre for Atmospheric Science, The University of Manchester, Oxford Road, Manchester, M13 9PL, United Kingdom

³ABB – Los Gatos Research, 3055 Orchard Drive, San Jose, CA 95134, California, United States of America

10 ⁴School of Mechanical, Aerospace and Civil Engineering, The University of Manchester, Oxford Road, Manchester, M13 9PL, United Kingdom

Correspondence to: Adil Shah (adil.shah@manchester.ac.uk)

Abstract. Methane emission fluxes from facility-scale sources may be poorly quantified, leading to uncertainties in the global methane budget. Accurate atmospheric measurement based flux quantification is urgently required to address this. This paper describes the test of a new near-field Gaussian plume inversion (NGI) technique, suitable for facility-scale flux quantification, using a controlled release of methane gas. Two unmanned aerial vehicle (UAV) platforms were used to perform 22 flight surveys downwind of a point-source release of methane gas from a regulated and flow-metered cylinder. One UAV was tethered to an instrument on the ground, while the other UAV carried an on-board high-precision prototype instrument, both of which used the same near-infrared laser technology. The performance of these instruments from UAV sampling is described. Both instruments were calibrated using certified standards, to account for variability in the instrumental gain factor. Furthermore, a modified approach to correcting for the effect of water vapour applied and is described here in detail. The NGI technique was used to derive emission fluxes for each UAV flight survey. We found good agreement of most NGI fluxes with the known controlled emission flux, within uncertainty, verifying the flux quantification methodology. The lower NGI flux uncertainty bound was, on average, $17\% \pm 10(1\sigma)\%$ of the controlled emission flux and the upper NGI flux uncertainty bound was, on average, $218\% \pm 100(1\sigma)\%$ of the controlled emission flux. These highly conservative uncertainty ranges incorporate factors including the variability in the position of the plume and the potential for under-sampling. While these average uncertainties are large compared to methods such as tracer dispersion, we suggest that UAV sampling can be highly complementary to a toolkit of flux approaches and may perform well in situations where site access for tracer release is problematic. We see tracer release applied to UAV sampling as an effective combination in future flux quantification studies. Successful flux quantification using this UAV sampling methodology demonstrates its future utility in identifying and quantifying emissions from methane sources such as oil and gas infrastructure facilities, livestock agriculture and landfill sites, where site access may be difficult.

1 Introduction

The global methane budget is subject to significant uncertainties (Kirschke et al., 2013; Saunio et al., 2016b; Nisbet et al., 2019), particularly from inventory uncertainty in facility scale sources such as landfill sites (Scheutz et al., 2009), herds of cattle (Blaxter and Clapperton, 1965) and oil and gas infrastructure (Brantley et al., 2014), which collectively contribute significantly to global methane emissions (Dlugokencky et al., 2011; Saunio et al., 2016a). These uncertainties can be reduced through the accurate source identification and subsequent quantification of methane emission fluxes using top-down (atmospheric measurements based) methods, in order to validate bottom-up (inventory based) emission flux estimates (Lowry et al., 2001; Nisbet and Weiss, 2010; Allen, 2016; Desjardins et al., 2018).

40



Accurate top-down flux quantification from facility scale sources requires a combination of wind vector measurements along with in situ measurements of atmospheric methane mole fraction (Dlugokencky et al., 1994; Rigby et al., 2017). Facility-scale emission fluxes can be derived from near-field sampling (less than 500 m from the source), which may be acquired from an unmanned aerial vehicle (UAV) platform (Gottwald and Tedders, 1985). UAVs are cheap, versatile and relatively
45 easy to use (Villa et al., 2016), compared to large manned aircraft (Illingworth et al., 2014; Lehmann et al., 2016). They can fly near to source and can be directed automatically using waypoints, to enable even and unbiased spatial sampling (Greatwood et al., 2017; Feitz et al., 2018). There are three principal approaches for measuring methane mole fraction from a UAV in situ: on-board air samples can be collected for subsequent analysis (Chang et al., 2016; Greatwood et al., 2017; Andersen et al., 2018), air can be pumped through a long tube to a sensor on the ground for analysis (Brosy et al., 2017;
50 Wolf et al., 2017; Shah et al., 2019) or air can be analysed live using a sensor mounted on-board the UAV (Berman et al., 2012; Khan et al., 2012; Nathan et al., 2015; Golston et al., 2017). Yet, a key limitation to accurate source identification and flux quantification is the precision of methane mole fraction measurements (Hodgkinson and Tatam, 2013). Miniaturised sensors suitable for UAV sampling are emerging (Villa *et al.*, 2016), but high precision lightweight in situ sensors, featuring superior techniques, such as off-axis integrated cavity output spectroscopy, have previously failed to materialise.

55

Some studies have also used UAV remote sensing measurements to derive emission fluxes (Golston et al., 2018; Yang et al., 2018). However, to our knowledge, only Nathan et al. (2015) have derived methane emission fluxes using UAV in situ measurements. In that study, a UAV with an on-board in-situ low precision sensor (± 0.1 ppm at 1 Hz) flew in orbits around a gas compressor station, using mass balance box modelling, with geospatial kriging for interpolation, to derive the emission
60 flux. However this method was not tested for UAV sampling using a (known) controlled release of methane gas, beforehand. It is crucial that novel flux quantification techniques are tested by sampling a controlled flux release, prior to investigating unknown emission sources (Desjardins et al., 2018; Feitz et al., 2018). Shah et al. (2019) were the first to test an in situ flux quantification technique using UAV sampling downwind of a controlled methane release. In that study, a UAV was connected to a high precision methane analyser on the ground using 150 m of tubing. Two-dimensional downwind sampling
65 on a vertical flux plane was used to develop the near-field Gaussian plume inversion (NGI) technique for flux quantification (Shah et al., 2019). Fully manual UAV piloting was employed in this previous study to actively pursue the position of the emission plume on the sampling plane, using mid-flight knowledge of its position. This resulted in calculated emission fluxes that were significantly positively biased compared to known emission fluxes; this represents a source of vulnerability in fully manual UAV sampling, which we address in this work.

70

Here we test the application of the NGI method with unbiased UAV sampling of controlled methane emission sources, by flying two UAVs downwind of the release. In this work, the causes of positive flux bias reported in Shah et al. (2019) were addressed in our sampling strategy, by flying a UAV without prior knowledge of the position of the emission plume. One UAV was connected to a commercially available instrument on the ground and the other carried a lighter prototype on-board
75 instrument (sect. 3). Both instruments were characterised and calibrated (sect. 2). Our modified approach to water vapour correction is also outlined in sect. 2. Sampled data was then used to derive NGI flux uncertainty ranges (sect. 4) for each of 22 flight surveys. In sect. 5 the success of the NGI method is assessed overall and its sampling constraints are summarised.



2 Methane instrumentation and calibration

2.1 Instrument inter-comparison

80 Two instruments were used to derive atmospheric methane mole fraction ($[X]$) measurements during UAV sampling. $[X]$ is
given in units of parts-per-million (ppm) throughout this paper, which are defined here as the number of moles of methane
per million moles of air ($10^{-6} \cdot \text{mol}_{\text{methane}} \text{mol}^{-1}$), with parts-per-million (ppb) defined as the number of moles of methane per
billion moles of air ($10^{-9} \cdot \text{mol}_{\text{methane}} \text{mol}^{-1}$). In this section, the ABB Los Gatos Research, Inc. Micro-portable Greenhouse
Gas Analyzer (MGGA) and a lighter prototype MGGA (pMGGA), designed for UAV use, are compared and characterised
85 to assess their performance. The technical specifications of both instruments are compared in Table 1. Both instruments use
off-axis integrated cavity output spectroscopy (ICOS) to derive simultaneous measurements of methane, carbon dioxide and
water mole fraction, from the absorption of a near-IR (1650 nm) laser. The pMGGA uses an additional laser to measure
carbon dioxide mole fraction more accurately. Off-axis ICOS techniques reflect a tuneable laser between two mirrors in a
high-finesse optical cavity, to obtain high-precision mole fraction measurements (see Paul et al. (2001) and Baer et al. (2002)
90 for further details on off-axis ICOS).

The e-folding time of the high-finesse cavity in both sensors was measured here by fitting an exponential decay function to
the transition from a high to low mole fraction standard gas (see Table 1 for results). This represents the time taken for
63.2% of the contents of the high-finesse cavity to be replaced. The Allan variance precision of each sensor was also derived
95 at various integration times, by measuring $[X]$ from a dry cylinder of compressed air for at least 17 hours of continuous
sampling (see Fig. S1 and Fig. S2 for Allan variance plots). The Allan deviation uncertainty factor (σ_{AV}), defined here,
represents the Allan deviation at the maximum sampling frequency. σ_{AV} for the MGGA and pMGGA are 2.71 ppm (at 10 Hz)
and 5.44 ppm (at 5 Hz), respectively, with the Allan deviation at 1 Hz and 0.1 Hz given in Table 1. The optimum Allan
variance integration time was also assessed for each sensor ((20 ± 3) s for the MGGA and (70 ± 10) s for the pMGGA); this
100 represents the maximum sampling time before instrumental drift begins to dominate over instrumental noise.

2.2 Water vapour correction

Raw wet methane mole fraction measurements ($[X]_0$) recorded by each instrument were corrected for the influence of
atmospheric water vapour, on mole fraction retrievals. Water vapour influences measurements of $[X]$ for three main reasons
(Karion et al., 2013; O'Shea et al., 2013; Rella et al., 2013). First and most significantly, dilution effects occur, where the
105 bulk presence of water reduces the quantity of methane in the cavity at a given pressure. Second, strong, broad infrared
absorption bands of water can lead to interference with the absorption spectrum of methane. Third, pressure broadening of
absorption peaks can occur, where collisional interaction between water and methane molecules changes the shape of the
methane spectral absorption band. These three effects have a net effect of decreasing $[X]_0$ in both instruments.

110 To account for these effects, both the MGGA and pMGGA use an internal retrieval algorithm to derive methane mole
fractions, which includes empirically-derived estimates of the pressure broadening coefficient in the presence of water
vapour. The instruments output both raw dry mole fraction measurements, which have additionally been corrected for the
effect of mole fraction dilution by water vapour, and raw wet methane mole fraction measurements ($[X]_0$) which have not
been corrected for this dilution effect (but are still calculated using the same empirically derived pressure broadening
115 coefficient). Typical pressure broadening coefficients are determined by the manufacturer based on experiments conducted
with a sample batch of instruments, yielding average values which are then applied to all instruments. However, because
these derived coefficients convolve line broadening due to water vapour with line broadening due to instrument factors, there



is some variability from unit to unit. Therefore, to obtain a more accurate correction for the influence of water vapour on the individual instruments used here, we apply a further post-processing correction factor to the $[X]_0$ measurements (without the dilution correction) reported by the instruments, using reported measurements of water mole fraction ($[\text{H}_2\text{O}]$).

Before a water correction could be applied, a $[\text{H}_2\text{O}]$ baseline ($[\text{H}_2\text{O}]_0$) was derived, as both instruments reported small, but non-zero values of $[\text{H}_2\text{O}]$, when sampling dry air. Gas from two cylinders with different methane compositions (1.901 ppm and 5.049 ppm) was dried by passing it through a dry ice water trap (a stainless-steel coil immersed in solid carbon dioxide pellets) before being sampled by both the MGGA and the pMGGA. Dry air from two additional cylinders (~104 ppm and 2.167 ppm) was also sampled by the MGGA. Each gas was sampled a minimum of 11 times for 4-minute periods, from which 1-minute averages were taken. $[\text{H}_2\text{O}]_0$ was observed to decay exponentially with dry uncalibrated methane mole fraction ($[X]_0^{\text{dry}}$), given by Eq. (1), where a is the water baseline offset, b is the water baseline coefficient and w is the water baseline decay factor. The plotted data used to fit $[\text{H}_2\text{O}]_0$ is given in Fig. S3 and Fig. S4.

$$(1) \quad [\text{H}_2\text{O}]_0 = a + \left(b \cdot e^{-\frac{[X]_0^{\text{dry}}}{w}} \right)$$

a , b and w for both instruments are given in Table 2. w for the pMGGA was assumed to be the same as w for the MGGA. The same w value was used for the pMGGA as gas was sampled by the MGGA at more $[X]_0^{\text{dry}}$ points, resulting in an improved fit.

Having established a well characterised water baseline, a post-processing water correction factor (v) was derived by sampling gas from a single cylinder, which was humidified to 9 fixed dew points (from 0 °C to 18 °C), using a dew point generator (LI-610, LI-COR, Inc.), following a similar experimental set-up used by O'Shea et al. (2013). The humidified gas was first sampled dry (to measure $[X]_0^{\text{dry}}$), by passing it through the dry ice water trap, and then sampled wet (to measure $[X]_0$ as a function of $[\text{H}_2\text{O}]$). An example of sampled $[X]_0$ and $[\text{H}_2\text{O}]$ measurements, used to calculate each data point, is given in Fig. S6.

$[X]_0$ is then corrected by dividing it by v , as v is effectively the ratio between $[X]_0$ and $[X]_0^{\text{dry}}$, as a function of $[\text{H}_2\text{O}]$. The ratio of $[X]_0$ to $[X]_0^{\text{dry}}$ was plotted against $([\text{H}_2\text{O}] - [\text{H}_2\text{O}]_0)$, where $[\text{H}_2\text{O}]_0$ was the water baseline measured during dry sampling (see Fig. S6 and Fig. S7). A quadratic fit was applied to both curves, with the intercept forced to unity. The first order coefficient (α) and second order coefficient (β) of the quadratic fit, given in Table 2, were then be used to derive v using Eq. (2), as a function of $[\text{H}_2\text{O}]$.

$$(2) \quad v = 1 + (\alpha \cdot ([\text{H}_2\text{O}] - [\text{H}_2\text{O}]_0)) + (\beta \cdot ([\text{H}_2\text{O}] - [\text{H}_2\text{O}]_0)^2)$$

As $[\text{H}_2\text{O}]_0$ in Eq. (2) is typically unknown, $[\text{H}_2\text{O}]_0$ defined in Eq. (1) can be substituted into Eq. (2), to yield Eq. (3).

$$(3) \quad v = 1 + \left(\alpha \cdot \left([\text{H}_2\text{O}] - a - \left(b \cdot e^{-\frac{[X]_0^{\text{dry}}}{w}} \right) \right) \right) + \left(\beta \cdot \left([\text{H}_2\text{O}] - a - \left(b \cdot e^{-\frac{[X]_0^{\text{dry}}}{w}} \right) \right)^2 \right)$$

As $[X]_0^{\text{dry}}$ in Eq. (3) is also unknown, an approximation that $[X]_0^{\text{dry}}$ is almost equal to $[X]_0$, in typical tropospheric humidity conditions, can be used. Thus Eq. (3) can be rewritten in terms of $[X]_0$ and $[\text{H}_2\text{O}]$, using Eq. (4).

$$(4) \quad v \approx 1 + \left(\alpha \cdot \left([\text{H}_2\text{O}] - a - \left(b \cdot e^{-\frac{[X]_0}{w}} \right) \right) \right) + \left(\beta \cdot \left([\text{H}_2\text{O}] - a - \left(b \cdot e^{-\frac{[X]_0}{w}} \right) \right)^2 \right)$$

To confirm the above assumption, as an example, when $[\text{H}_2\text{O}]$ is 0.01 mol_{water} mol⁻¹ and $[X]_0^{\text{dry}}$ is 5 ppm, Eq. (3) yields v of 0.98089 and Eq. (4) yields a similar value for v of 0.98085, for the MGGA.

155



The uncertainty in the water correction was quantified using the water correction residual (R) from Eq. (2), to derive a water uncertainty factor (σ_v) for each instrument (see Table 2).

$$(5) \quad \sigma_v = \left(\frac{\sum(R^2)}{N} \right)^{\frac{1}{2}}$$

160 N is the total number of residuals. Using the above to correct for the effects of water vapour in the measurement cavity, we can increase the accuracy of $[X]_0$ measurements. For example our correction was used to increase the MGA measurement accuracy of $[X]_0$ (at 2 ppm) by +0.27%, at a humidity of $0.001 \text{ mol}_{\text{water}} \text{ mol}^{-1}$, and by +1.8%, at a humidity of $0.01 \text{ mol}_{\text{water}} \text{ mol}^{-1}$.

2.3 Calibration

165 In order to convert $[X]_0$ into $[X]$, both instruments were calibrated by sampling gas from two cylinders: one contained a low standard methane mole fraction ($[X]_{\text{low}}$) of 1.901 ppm and the other contained a high standard methane mole fraction ($[X]_{\text{high}}$) of 5.049 ppm. The composition of both cylinders was certified such that they were referenceable to the World Meteorological Organisation Greenhouse Gas Scale (WMO-X2004A). Each gas was sampled intermittently for 4-minute periods of continuous sampling. The dry ice water trap was used throughout each calibration, to ensure dry gas entered the sensor cavities.

170 One-minute averages from each 4-minute sampling period were taken to derive one value of low $[X]_0^{\text{dry}}$ ($[X]_0^{\text{dry}}_{\text{low}}$) and one value of high $[X]_0^{\text{dry}}$ ($[X]_0^{\text{dry}}_{\text{high}}$) representative for each 8-minute period. The time increment between each $[X]_0^{\text{dry}}_{\text{low}}$ and $[X]_0^{\text{dry}}_{\text{high}}$ value was then interpolated from 8 minutes to 4 minutes, such that every measured value of $[X]_0^{\text{dry}}_{\text{low}}$ had a corresponding interpolated value of $[X]_0^{\text{dry}}_{\text{high}}$ and vice-versa. Individual measured and interpolated values of $[X]_0^{\text{dry}}_{\text{low}}$ and
175 $[X]_0^{\text{dry}}_{\text{high}}$ for both instruments are plotted in Fig. S8 and Fig. S9. These measured and interpolated averages were used to calculate an average gain factor (G) and gain factor uncertainty (σ_G), from the average and standard deviation, respectively, using a set of at least 24 individual gain factors, calculated using Eq. (6) (Pitt et al., 2016).

$$(6) \quad \text{gain factor} = \frac{[X]_{\text{high}} - [X]_{\text{low}}}{[X]_0^{\text{dry}}_{\text{high}} - [X]_0^{\text{dry}}_{\text{low}}}$$

180 The average offset (C) and offset uncertainty (σ_C) was calculated by taking the average and standard deviation, respectively, of individual offsets, calculated using Eq. (7) and Eq. (8) (Pitt et al., 2016).

$$(7) \quad \text{low offset} = [X]_{\text{low}} - (G \cdot [X]_0^{\text{dry}}_{\text{low}})$$

$$(8) \quad \text{high offset} = [X]_{\text{high}} - (G \cdot [X]_0^{\text{dry}}_{\text{high}})$$

G , σ_G , C and σ_C for both instruments are given in Table 3.



185 A key advantage of this calibration procedure is that the uncertainty in G is well quantified up to $[X]_{\text{high}}$ (for stable
temperature and pressure) and can be incorporated in the measurement uncertainty. Separate in-field calibrations would be
preferable to enhance measurement accuracy, by accounting for variability in temperature and pressure. However there are
logistical challenges with in-field calibrations, such as the need for calibration gases and the time required to perform
calibrations in dynamic atmospheric temperature and pressure conditions. The laboratory calibrations described here
190 required at least three hours of sampling in order to characterise the variability in G : this may be impractical in field
conditions. Therefore the calibration coefficients presented here are useful as they account for variability in G under
laboratory conditions.

2.4 Methane enhancement and uncertainty

The calibration and water vapour correction procedures described above show that G is almost equal to 1, C is almost equal
195 to 0 (see Table 3) and v is almost equal to 1 (at 5 ppm methane and a very high $0.01 \text{ mol}_{\text{water}} \text{ mol}^{-1}$ humidity) for both
instruments. This means that both instruments record raw $[X]_0$ measurements with very little systematic error, even when
uncalibrated. Thus for most methane measurement purposes, $[X]_0$ may not need to be corrected. However in this work, G and
 v were applied to $[X]_0$ for optimal instrumental accuracy.

200 $[X]$ can be calculated in ppm using Eq. (9).

$$(9) \quad [X] = \left(\frac{G}{v}\right) \cdot [X]_0 + C$$

However, during flux calculation, the enhancement in methane mass density (E), in kg m^{-3} , above some background is
required and was calculated here using Eq. (10). The background methane mole fraction ($[X]_b$) and corresponding
background uncertainty (σ_b) can be calculated from a subset of $[X]_0$ measurements, which can be acquired from out-of-plume
205 sampling (see Sect. 3). The molar density of air (ρ) and the uncertainty in ρ (σ_ρ), in units of mol m^{-3} , can be derived from
pressure and temperature measurements. The molar mass of methane (M) is fixed at $0.01604 \text{ kg mol}_{\text{methane}}^{-1}$.

$$(10) \quad E = ([X]_0 - [X]_b) \cdot \frac{G}{v} \cdot \rho \cdot M$$

The uncertainty in E (σ_E) can be calculated by combining σ_b with the precision and accuracy uncertainty components of $[X]$,
using Eq. (11). Precision is characterised by σ_{AV} and accuracy is characterised by σ_G and σ_v terms.

$$210 \quad (11) \quad \sigma_E = E \cdot \left(\left(\left(\sigma_{AV}^2 + \left(\sigma_b \cdot \frac{G}{v} \right)^2 \right) \cdot \left(\frac{\rho \cdot M}{E} \right)^2 \right) + \left(\frac{\sigma_G}{G} \right)^2 + \left(\frac{\sigma_v}{v} \right)^2 + \left(\frac{\sigma_\rho}{\rho} \right)^2 \right)^{\frac{1}{2}}$$

Although M remains constant, v in Eq. (11) changes as a function of $[X]_0$ and $[\text{H}_2\text{O}]$, for each value of E . σ_C is not required in
Eq. (11) as the offset cancels out in Eq. (10). This is an important advantage of calculating E rather than $[X]$, during the flux
analysis used in the following section.

3 Method Testing

215 3.1 Experimental description

A UAV sampling methodology for source identification and flux quantification was tested in two fields adjacent to a natural
gas extraction facility in Little Plumpton (near Wesham), Lancashire, United Kingdom (+53.78785° N, -2.94758° E), prior
to any drilling or hydraulic fracturing, over five sampling days in August and September 2018. A map of the field site is
given in Fig. 1. The two adjacent grass fields, in which all UAV sampling took place, belong to a fully operational dairy
220 farm. Methane was released from within the operating site at one of two controlled flux rates (F_0), from 0.25 m above



ground level (see SI for controlled release details). F_0 was undisclosed during flux analysis, prior to the comparisons shown later in this paper, allowing for blind method testing.

225 Two adapted DJI Spreading Wings S1000+ octocopter UAVs (labelled UAV1 and UAV2) were used to sample the methane
plume on a downwind vertical plane, roughly perpendicular to mean wind direction (see Table 4 for UAV details).
Measurements of $[X]$ from both platforms are given in Fig. 2. UAV1 was operated using pre-programmed waypoints and
ascended diagonally. Each UAV1 flight survey was composed of two parts: one flight to the right of the source (projected
onto the sampling plane, perpendicular to mean wind direction) and one to the left. Meanwhile each UAV2 flight survey was
composed of a single flight, to perform horizontal transects, each transect at a roughly fixed height, up to approximately
230 100 m laterally away from the take-off position. 7 surveys were conducted by UAV1 (labelled, T1.1 – T1.7) and 15 surveys
were conducted by UAV2 (labelled, T2.1 – T2.15). Individual flight survey details are given in Table S1 and Table S2.

UAV1 was connected to the MGGA on the ground, using 150 m of perfluoroalkoxy (PFA) tubing (4.76 mm inner diameter;
6.35 mm outer diameter). Air was pulled through the tubing using a small pump (NMS 030.1.2 DC-B 12V, KNF Neuberger
235 UK Ltd), from which the MGGA subsampled. The sampling lag time between air entering the air inlet at the end of the tube
on the UAV and air entering the MGGA cavity was measured to be 25 s. Both the MGGA and the pump were powered by a
12 V lead-acid battery. As the tether connected to UAV1 occasionally kinked during flight, blocking air through the tube,
there were periods of $[X]_0$ sampling that were omitted from each flight (such periods were identified and recorded in the field
from the flow of air to the pump). The pMGGA was mounted on board UAV2, beneath the centre frame. The sampling lag
240 time between air entering the external air inlet and air entering the pMGGA cavity was measured to be 2 s. The pMGGA was
powered using the on-board 22.2 V UAV2 battery. Both the MGGA and pMGGA transmitted live, real-time mole fraction
measurements wirelessly, to a tablet computer on the ground. Satellite geolocation was recorded by the pMGGA, on-board
UAV2, simultaneous with every $[X]_0$ measurement. Satellite geolocation was recorded on UAV1 by a separate on-board
computer, sampling at 1 Hz. Aerial plots of UAV flight tracks are given in Fig. S10 for UAV1 and Fig. S11 for UAV2.

245 A lightweight wind sensor (FT205EV, FT Technologies Limited) was mounted on-board UAV1, on a carbon fibre pole
305 mm above the plane of the propellers. It recorded wind speed and direction at 4 Hz. This data was used to model the
change in wind speed with height above ground level (z). A two-dimensional stationary sonic anemometer (WS500-UMB
Smart Weather Sensor, G. Lufft Mess- und Regeltechnik GmbH) was also situated on the southern boundary of the operating
250 site (see Fig. 1), (3.30±0.03) m above ground level. This provided wind speed, wind direction, temperature and pressure
measurements every minute. Wind measurements from both sensors were combined to derive the average absolute wind
speed as a function of z ($WS(z)$), for the duration of each flight survey. This is described in detail in the SI.

3.3 Flux density measurements

Each UAV1 survey resulted in $(9±1(1σ))$ minutes of useable $[X]_0$ measurements and each UAV2 survey resulted in
255 $(8±1(1σ))$ minutes of useable $[X]_0$ measurements (see Table S1 and Table S2 for individual sampling periods). This data was
prepared for flux quantification by carrying out the following steps. The $[X]_0$ timestamp from both instruments was corrected
to account for lag time. 1 Hz satellite geolocation from UAV1 was interpolated to the 10 Hz $[X]_0$ frequency of the MGGA. E
was calculated with $[X]_0$ measurements from both instruments using Eq. (10). $[X]_b$ was derived by fitting a log-normal
distribution to all recorded $[X]_0$ measurements from each flight survey, using the method described by Shah et al. (2019).
260 This background was derived from a histogram of all useable $[X]_0$ measurements acquired during each flight experiment; a
log-normal fit can usually be applied to the lowest $[X]_0$ measurements in the histogram, which represent out-of-plume
sampling. The peak of the log-normal fit to these lowest $[X]_0$ measurements was taken to be $[X]_b$. $ρ$ was derived using



average temperature and pressure recorded by the stationary anemometer for the duration of each flight survey, with the standard deviation in temperature and pressure used to derive σ_p .

265

Satellite-derived altitude was corrected to obtain the height of the air inlet above ground level, by taking into account take-off altitude and the height of the air inlet when on the ground. This step ensures that the data represent the true point of sampling. After converting longitude and latitude from degrees into meters, metric longitude and latitude were projected onto a plane perpendicular to and a plane parallel to mean wind direction. Mean wind direction was derived from the stationary anemometer for the duration of each flight survey. The coordinate projection procedure is described in further detail by Shah et al. (2019).

270

In order to calculate flux, flux density, q , (in $\text{kg s}^{-1} \text{m}^{-2}$) was derived. To achieve this, each geospatially mapped E measurement was combined with $WS(z)$, using Eq. (12).

275

$$(12) \quad q = E \cdot WS(z)$$

Geospatially mapped q , on a plane perpendicular to mean wind direction, for each flight survey, is given in Fig. 3 for UAV1 and in Fig. 4 for UAV2. Measurements of $[X]$ (see Fig. 2) were not used in the flux analysis, but are nevertheless of interest, as they show $[X]$ to generally reduce with z , as expected, to support observations of enhancements in q shown in Fig. 3 and Fig. 4.

280

Both Fig. 3 and Fig. 4, show significant background sampling (yellow data points), extending sufficiently far away from the position of the source projected onto the sampling plane (0 m), such that the plume centre across each transect (manifested by a peak mole fraction) had been passed. All of the UAV1 surveys in Fig. 3 took place from a similar distance from the source, of approximately 50 m. It is clear that during most UAV1 surveys, enhancements in q were concentrated near the ground (below 10 m) and close to the position of the source, projected onto the sampling plane. However T1.3 shows considerable enhancements in q above the ground (up to approximately 30 m), which was possibly due to a transient updraft. Meanwhile, the UAV2 flight surveys in Fig.4, many of which took place approximately 100 m from the source, show large enhancements in q across the flux plane, up to approximately 15 m above the ground. Enhancements of q in Fig. 4 can also be seen at a much greater lateral distance from the source, projected onto the sampling plane. This is likely a consequence of many UAV2 flight surveys sampling at a greater distance from the source than UAV1 flight surveys, which gave the plume more time to spread out.

285

290

3.4 Flux quantification

Calculated flux density (q) from each flight survey was used to derive an emission flux (in units of kg s^{-1}) using the near-field Gaussian plume inversion (NGI) flux quantification technique (see Shah et al. (2019)). In principle, the NGI method accounts for turbulent variations in wind using Gaussian statistics. The method also takes into account sampling on a slightly offset sampling plane (compared to the plane perpendicular to mean wind direction) by introducing a third dimension to the traditional two-dimensional Gaussian plume model. The NGI method uses a least-squares approach to compare measured and modelled values of q . Residuals in q are minimised to output model parameters, which include an initial flux estimate (F_e).

295

300

Full details of the NGI method can be found in Shah et al. (2019). We provide a brief overview here. The size of the plume is assumed to increase linearly with distance from the source, by assuming q to decrease according to the inverse square law with distance (an assumption which is valid over short distances). Therefore instead of using constant crosswind and vertical dispersion terms, these terms are allowed to increase with distance from the source, with both terms being fixed at a one



305 metre distance. The crosswind dispersion term (at 1 m) is characterised using measurements of q , rather than assumptions of
atmospheric stability, as these assumptions are valid for plumes characterised by dispersion, rather than turbulent advection.
In addition, the centre of the plume in the crosswind direction is derived from measurements of q , as the precise position of
the source may be unknown. The vertical dispersion term (at 1 m) and F_e can then be acquired by inverting modelled values
of q , derived by minimising residuals, as described above.

310 A measurement flux uncertainty (σ_F) is calculated by combining the uncertainties in individual E , $u(z)$ and $v(z)$ values. A
lower uncertainty bound (σ^-) is calculated using residuals between modelled and measured q values. An upper uncertainty
bound (σ^+) is calculated by incorporating σ^- with the potential effects of negative flux bias due to under-sampling, using a
random walk simulation. The simulation is repeated 180 times for each flight survey. In each simulation, a static Gaussian
315 plume (simulating a prescribed arbitrary target flux) is sampled across three dimensions, where sampling is constrained to
the spatial limits of UAV sampling and is limited to the UAV sampling duration. The NGI method is used to derive a flux
from these random walk simulations. The average fractional target flux underestimation from these simulations can be
incorporated into σ^+ . Random walk flux underestimation occurs due to limited spatial sampling coverage (i.e. sampling gaps)
and limited spatial sampling extent. This simulation step therefore gives an important indication of the systematic error due
320 to potential under-sampling. All F_e , σ^- , σ^+ and σ_F values for each flight survey are given in Table S5.

4 Flux results and discussion

Calculated NGI emission fluxes were compared to the known (controlled) emission fluxes, using the ratio between the NGI
flux uncertainty range and F_0 (see Fig. 5). As this was a blind flux analysis, F_0 was not revealed to the analysis team
researchers prior to calculating the flux uncertainty range. Fig. 5 shows that the NGI flux uncertainty range agrees well with
325 F_0 , for most flight surveys. Only four surveys (T2.1, T1.1, T1.3 and T1.7) had a flux uncertainty range that fell short of F_0 .
Although no flux uncertainty range exceeded F_0 , T2.3 spanned a large flux range, much of which fell above F_0 . Flux
underestimation may be explained using the plots shown in Fig. 3 and Fig. 4, which demonstrate the following: a limited
sampling duration made it possible to almost entirely avoid the emission plume, thus resulting in low flux results; similarly,
some flights intersected the emission plume multiple times resulting in flux overestimation in cases, although large NGI
330 uncertainty ranges can conservatively account for this effect. Therefore it is clear that the F_e value obtained using the NGI
method must not be taken at face value and the full NGI flux uncertainty range must be considered. Furthermore, the flux
ranges in Fig. 5 represent uncertainty bounds of one standard deviation; it is statistically realistic to expect some discrepancy
between F_0 and the NGI flux uncertainty range.

335 The flux uncertainty ranges given in Fig. 5 are asymmetric, although the magnitude of this asymmetry was different for
flight experiments conducted by the different UAVs. σ^+ was $(0.33 \pm 0.13(1\sigma))$ times larger than σ^- for UAV2 but was only
 $(0.06 \pm 0.03(1\sigma))$ times larger for UAV1. This is because UAV2 sampled further from the source, on average, on a similar
sized sampling plane to UAV1. As UAV2 was further from the emission source, the instantaneous plume had a greater
likelihood of extending beyond the sampling plane and being missed (beyond the horizontal edges of the sampling plane),
340 due to spatially limited sampling. This potential loss of in-plume sampling may have otherwise contributed towards the
overall flux, thus enhancing σ^+ . Therefore σ^+ is comparatively larger than σ^- for flights conducted by UAV2.

It is important to recognise the magnitude of the NGI uncertainty ranges in Fig. 5, relative to F_0 , which are due to the
difficulties in inverting sparse spatial sampling to derive an emission flux, following the NGI method. These uncertainties
345 reflect the limited duration of sampling and the effects of variability in wind. While we fully acknowledge that flux



uncertainty ranges in Fig. 5 are large, we believe that the true value of the NGI method with UAV sampling is to derive snap-shot rapid flux estimates at low cost, with an order-of-magnitude level precision, for subsequent flux investigation using more precise flux quantification techniques. Although longer periods of sampling in each flight survey may reduce the uncertainties in Fig. 5, this is practically difficult with limited UAV battery life, with little additional benefit. Tethered power or multiple UAV flights may alternatively be used, as was the case with UAV1, but wind conditions can quickly change when sampling for prolonged periods with too many lengthy intervals between flights.

In order to assess whether multiple flight surveys could be used effectively to capture the known controlled emission flux, within uncertainty, the upper and lower NGI uncertainty bounds were averaged for all surveys (see penultimate row of Fig. 5). The average lower NGI flux uncertainty bound as a fraction of F_0 (\bar{F}_-) was $0.2 \pm 0.1(1\sigma)$ and the average upper NGI flux uncertainty bound as a fraction of F_0 (\bar{F}_+) was $2 \pm 1(1\sigma)$, for all surveys. Thus F_0 (i.e. 1 in Fig. 5) falls comfortably within the average NGI flux uncertainty range, over 22 independent flight surveys. \bar{F}_- and \bar{F}_+ were also calculated for surveys conducted by UAV1 and UAV2, separately. These separate \bar{F}_- and \bar{F}_+ values for each UAV comfortably overlap with the \bar{F}_- and \bar{F}_+ values for all surveys combined. This suggests that the sampling strategies employed by UAV1 and UAV2 were both capable of deriving the known emission flux, with a similar degree of both lower and upper uncertainty. The percentage standard error in \bar{F}_- and \bar{F}_+ , over all 22 flight surveys, was 13% and 10%, respectively. The large standard errors in \bar{F}_- and \bar{F}_+ may be reduced with more surveys, in order to better constrain the NGI flux uncertainty range. However more precise flux estimates can be obtained with the tracer dispersion methods. Although we recognise that the \bar{F}_- and \bar{F}_+ uncertainty averages are large, we emphasise that our methodology has been adapted for rapid flux analysis, rather than precise flux estimates for inventory publication.

The ability of the NGI method to calculate a target emission flux was further assessed by calculating the central flux estimate as a fraction of F_0 (F_c) for each flight survey, using Eq. (13). F_c is distinct from F_e (as a fraction of F_0), in that F_c finds the centre of an asymmetric flux uncertainty, whereas F_e is an initial flux estimate calculated using the NGI method, which does not take into account the potential effects of under-sampling, which may result in a potential negative flux bias.

$$(13) \quad F_c = \frac{F_e + \left(\frac{\sigma_+ - \sigma_-}{2}\right)}{F_0}$$

The mean of F_c (\bar{F}_c) and the mean standard error in \bar{F}_c for the 22 surveys (see bottom row of Fig. 5) treats each survey as an independent quantification of the flux, with no weighting for sampling time (as flight times were broadly similar). This clearly demonstrates the improvement in flux accuracy (for a constant source) that can be obtained with greater sampling time or repeated flights, as expected. \bar{F}_c was also calculated for surveys conducted by UAV1 and UAV2 separately: these separate \bar{F}_c values both overlap with the combined \bar{F}_c value for all flight surveys (within one standard deviation); there is no discernible difference in the NGI flux result results obtained by either UAV. This suggests that both UAV sampling strategies were equally capable of delivering the same emission flux estimate, by taking the average of multiple flight surveys.

The overlap of the standard deviation in \bar{F}_c (shown in Fig. 5) with the known emission flux (i.e. 1 in Fig. 5) also suggests that there was no apparent flux bias (within uncertainty) in this study. This indicates that we have successfully overcome the causes of positive biases reported by Shah et al. (2019). Shah et al. (2019) sampled downwind of a controlled emission source and actively pursued the emission plume (projected onto the sampling plane) using mid-flight knowledge of its position, inferred by releasing smoke grenades during flight surveys. However in this work, manual sampling was avoided



by either flying UAV1 using pre-programmed waypoints or by flying UAV2 using lateral transects in course-lock. Both approaches successfully avoided biased sampling.

390 To conclude, UAV sampling can be used to practically derive unbiased snap-shot emission fluxes with the NGI method, with
an order-of-magnitude precision, by sampling on a plane perpendicular to wind direction from at least approximately 50 m
away from the source. Although typical flux uncertainties were high, NGI UAV fluxes serve as an important tool for snap-
shot source identification and flux quantification. Our UAV methodology fills an important gap between cheap leak
detection techniques (such as infrared cameras), which do not provide fluxes, and reliable flux quantification techniques
(such as the tracer dispersion method), which require expensive instrumentation and may be more difficult to organise. For
395 example, tracer methods can be problematic in cases where site access for tracer release is impossible or in cases where the
plume may be lofted. The UAV methodology we describe is highly suitable for leak detection and source isolation, for
regulatory leak detection, with the added capability to gauge the severity of flux leaks, for subsequent investigation using
other approaches. We anticipate a combination of UAV sampling with a tracer release, where both a target gas (in this case
methane) and a proxy tracer can be measured simultaneously downwind, taking advantage of vertical sampling enabled by
400 UAVs, as a powerful future toolkit for precise flux quantification.

5 Conclusions

Two UAVs were used to test the near-field Gaussian plume inversion technique for flux quantification. One UAV was
connected to the MGGGA on the ground using a tether, while the other carried a new ABB pMGGGA prototype instrument on-
board. Both instruments measured atmospheric methane mole fraction, which was calibrated and corrected for the influence
405 of water vapour, following laboratory testing.

The flux approach was tested for 22 UAV flight surveys, by deriving fluxes from a controlled release of methane gas. This
yielded successful results, with 18 out of 22 fluxes falling within the UAV-derived flux uncertainty range. This demonstrates
that the near-field Gaussian plume inversion methodology used here could be used to derive emission fluxes from UAV
410 sampling of plumes from facility-scale (point) sources, where such sources are relatively invariant over the period of such
UAV sampling. The lower flux uncertainty bound was, on average, $17\% \pm 10(1\sigma)\%$ of the controlled emission flux and the
upper flux uncertainty bound was, on average, $218\% \pm 100(1\sigma)\%$ of the controlled emission flux. Thus the known emission
flux was comfortably encapsulated by the UAV flux results, within uncertainty.

415 A key advantage of the methodology used here is the ability to sample downwind of sources to obtain off-site mole fraction
measurements. Such sampling allows for independent and portable studies of methane emissions without the need for heavy
infrastructure, special permissions, runway access or prior notification. We conclude that the near-field Gaussian plume
inversion flux method can be used confidently in future with UAV sampling to derive snap-shot methane emission fluxes
from relatively constant facility-scale sources such as oil and gas infrastructure, livestock agriculture and landfill sites. An
420 exciting future application may be the incorporation of UAV sampling within the tracer release method, where simultaneous
measurement of a target gas and a proxy tracer can take advantage of vertical sampling enabled by UAVs. This avoids the
limitation of current mobile vehicle sampling which cannot sample lofted plumes. Together, this may represent a powerful
future toolkit for precise and efficient flux quantification.



Author contribution

425 AS, JRP, HR, JBL, PIW and GA carried out the field experiments. All authors designed the field experiments. AS and JRP carried out and designed the laboratory experiments. AS, JRP and JBL developed the sensor characterisation procedures. JBL provided access to the prototype sensor. AS wrote the manuscript. GA edited the manuscript. All authors contributed towards the manuscript.

Acknowledgments

430 Adil Shah's PhD is funded by the Natural Environment Research Council (NERC), grant reference NE/L002469/1, and is supported through a CASE partnership with the Environment Agency. NERC also provided contributions, in kind, through EQUIPT4RISK, grant reference NE/R01809X/1. We thank ABB – Los Gatos Research for loaning us the pMGGA. We also thank the farmer for allowing us to operate on his land and Cuadrilla Resources Ltd. for facilitating access.

References

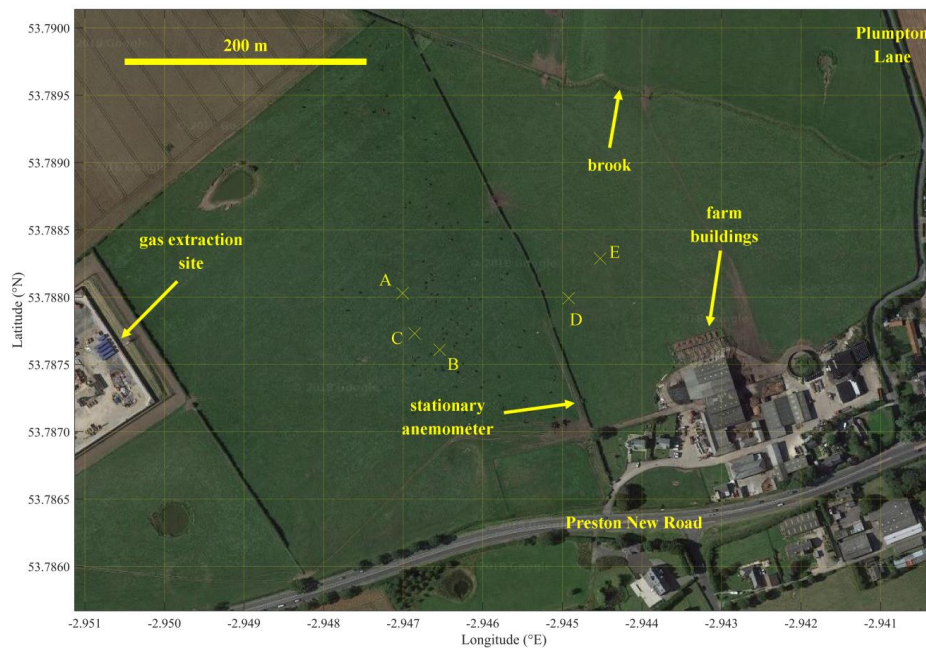
- 435 Allen, G.: Rebalancing the global methane budget, *Nature*, 538, pp.46-48, 2016.
- Andersen, T., Scheeren, B., Peters, W., and Chen, H.: A UAV-based active AirCore system for measurements of greenhouse gases, *Atmos Meas Tech*, 11, pp.2683-2699, 10.5194/amt-11-2683-2018, 2018.
- Baer, D. S., Paul, J. B., Gupta, M., and O'Keefe, A.: Sensitive absorption measurements in the near-infrared region using off-axis integrated-cavity-output spectroscopy, *Appl Phys B-Lasers O*, 75, pp.261-265, 10.1007/s00340-002-0971-z, 2002.
- 440 Berman, E. S. F., Fladeland, M., Liem, J., Kolyer, R., and Gupta, M.: Greenhouse gas analyzer for measurements of carbon dioxide, methane, and water vapor aboard an unmanned aerial vehicle, *Sensor Actuat B-Chem*, 169, pp.128-135, 10.1016/j.snb.2012.04.036, 2012.
- Blaxter, K. L., and Clapperton, J. L.: Prediction of the amount of methane produced by ruminants, *British Journal of Nutrition*, 19, pp.511-522, 10.1079/BJN19650046, 1965.
- 445 Brantley, H. L., Thoma, E. D., Squier, W. C., Guven, B. B., and Lyon, D.: Assessment of Methane Emissions from Oil and Gas Production Pads using Mobile Measurements, *Environ Sci Technol*, 48, pp.14508-14515, 10.1021/es503070q, 2014.
- Brosy, C., Krampf, K., Zeeman, M., Wolf, B., Junkermann, W., Schäfer, K., Emeis, S., and Kunstmann, H.: Simultaneous multicopter-based air sampling and sensing of meteorological variables, *Atmos Meas Tech*, 10, pp.2773-2784, 10.5194/amt-10-2773-2017, 2017.
- 450 Chang, C. C., Wang, J. L., Chang, C. Y., Liang, M. C., and Lin, M. R.: Development of a multicopter-carried whole air sampling apparatus and its applications in environmental studies, *Chemosphere*, 144, pp.484-492, 10.1016/j.chemosphere.2015.08.028, 2016.
- Desjardins, R. L., Worth, D. E., Pattey, E., VanderZaag, A., Srinivasan, R., Mauder, M., Worthy, D., Sweeney, C., and Metzger, S.: The challenge of reconciling bottom-up agricultural methane emissions inventories with top-down measurements, *Agr Forest Meteorol*, 248, pp.48-59, 10.1016/j.agrformet.2017.09.003, 2018.
- 455 Dlugokencky, E. J., Steele, L. P., Lang, P. M., and Masarie, K. A.: The growth rate and distribution of atmospheric methane, *J Geophys Res-Atmos*, 99, pp.17021-17043, 10.1029/94jd01245, 1994.
- Dlugokencky, E. J., Nisbet, E. G., Fisher, R., and Lowry, D.: Global atmospheric methane: budget, changes and dangers, *Philos T R Soc A*, 369, pp.2058-2072, 10.1098/rsta.2010.0341, 2011.
- 460 Feitz, A., Schroder, I., Phillips, F., Coates, T., Negandhi, K., Day, S., Luhar, A., Bhatia, S., Edwards, G., Hrabar, S., Hernandez, E., Wood, B., Naylor, T., Kennedy, M., Hamilton, M., Hatch, M., Malos, J., Kochanek, M., Reid, P., Wilson, J., Deutscher, N., Zegelin, S., Vincent, R., White, S., Ong, C., George, S., Maas, P., Towner, S., Wokker, N., and Griffith, D.:



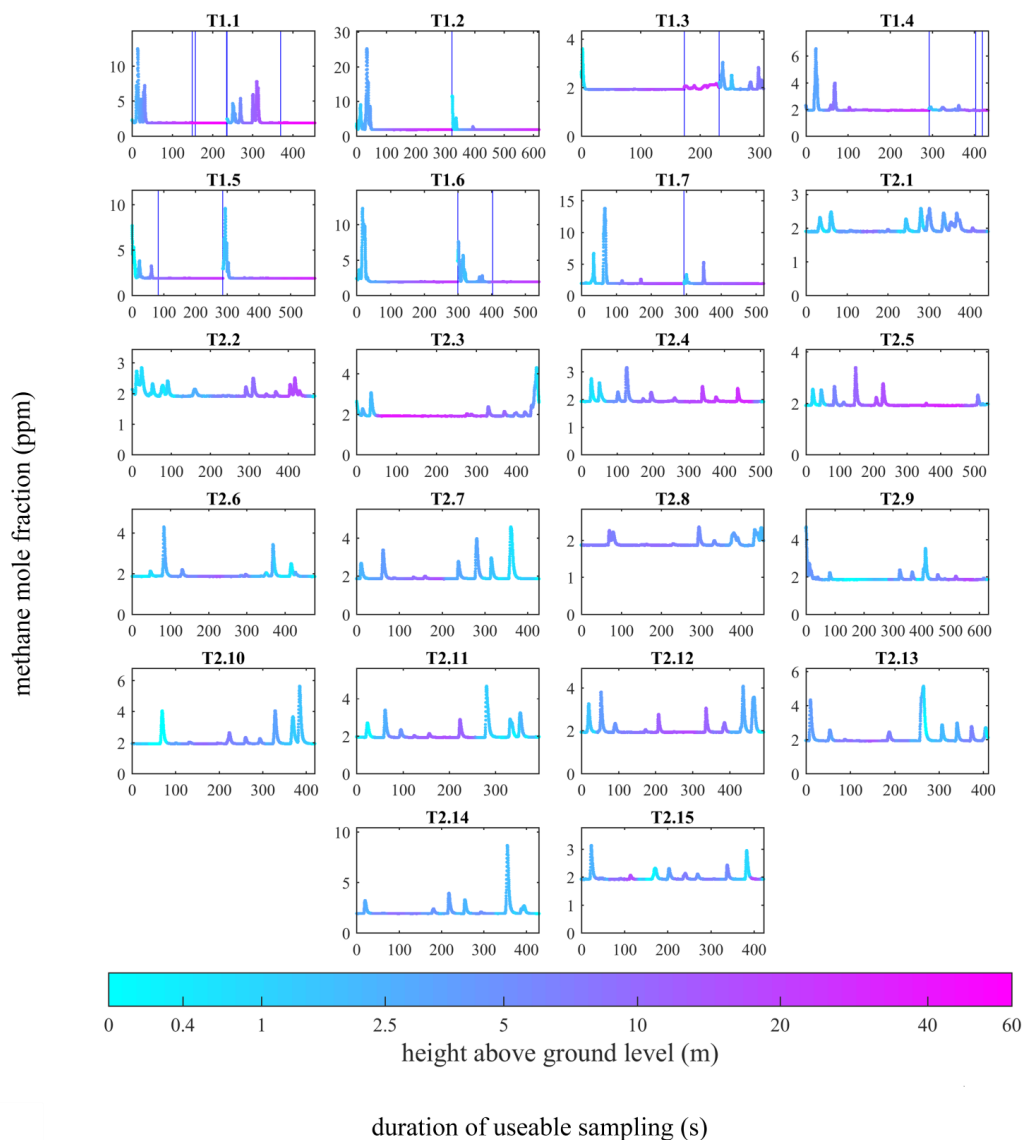
- The Ginninderra CH₄ and CO₂ release experiment: An evaluation of gas detection and quantification techniques, *Int J Greenh Gas Con*, 70, pp.202-224, 10.1016/j.ijggc.2017.11.018, 2018.
- 465 Golston, L. M., Tao, L., Brosy, C., Schäfer, K., Wolf, B., McSpirtt, J., Buchholz, B., Caulton, D. R., Pan, D., Zondlo, M. A., Yoel, D., Kunstmann, H., and McGregor, M.: Lightweight mid-infrared methane sensor for unmanned aerial systems, *Appl Phys B-Lasers O*, 123, article number: 170, 10.1007/S00340-017-6735-6, 2017.
- Golston, L. M., Aubut, N. F., Frish, M. B., Yang, S. T., Talbot, R. W., Gretencord, C., McSpirtt, J., and Zondlo, M. A.: Natural Gas Fugitive Leak Detection Using an Unmanned Aerial Vehicle: Localization and Quantification of Emission Rate, *Atmosphere-Basel*, 9, article number: 333, 10.3390/Atmos9090333, 2018.
- 470 Gottwald, T. R., and Tedders, W. L.: A Spore and Pollen Trap for Use on Aerial Remotely Piloted Vehicles, *Phytopathology*, 75, pp.801-807, 10.1094/Phyto-75-801, 1985.
- Greatwood, C., Richardson, T. S., Freer, J., Thomas, R. M., MacKenzie, A. R., Brownlow, R., Lowry, D., Fisher, R. E., and Nisbet, E. G.: Atmospheric Sampling on Ascension Island Using Multirotor UAVs, *Sensors-Basel*, 17, article number: 1189, 10.3390/S17061189, 2017.
- 475 Hodgkinson, J., and Tatam, R. P.: Optical gas sensing: a review, *Meas Sci Technol*, 24, article number: 012004, 10.1088/0957-0233/24/1/012004, 2013.
- Illingworth, S., Allen, G., Percival, C., Hollingsworth, P., Gallagher, M., Ricketts, H., Hayes, H., Ładosz, P., Crawley, D., and Roberts, G.: Measurement of boundary layer ozone concentrations on-board a Skywalker unmanned aerial vehicle, *Atmos Sci Lett*, 15, pp.252-258, 10.1002/asl2.496, 2014.
- 480 Karion, A., Sweeney, C., Wolter, S., Newberger, T., Chen, H., Andrews, A., Kofler, J., Neff, D., and Tans, P.: Long-term greenhouse gas measurements from aircraft, *Atmos Meas Tech*, 6, pp.511-526, 10.5194/amt-6-511-2013, 2013.
- Khan, A., Schaefer, D., Tao, L., Miller, D. J., Sun, K., Zondlo, M. A., Harrison, W. A., Roscoe, B., and Lary, D. J.: Low Power Greenhouse Gas Sensors for Unmanned Aerial Vehicles, *Remote Sens-Basel*, 4, pp.1355-1368, 10.3390/rs4051355, 2012.
- 485 Kirschke, S., Bousquet, P., Ciais, P., Saunoy, M., Canadell, J. G., Dlugokencky, E. J., Bergamaschi, P., Bergmann, D., Blake, D. R., Bruhwiler, L., Cameron-Smith, P., Castaldi, S., Chevallier, F., Feng, L., Fraser, A., Heimann, M., Hodson, E. L., Houweling, S., Josse, B., Fraser, P. J., Krummel, P. B., Lamarque, J. F., Langenfelds, R. L., Le Quere, C., Naik, V., O'Doherty, S., Palmer, P. I., Pison, I., Plummer, D., Poulter, B., Prinn, R. G., Rigby, M., Ringeval, B., Santini, M., Schmidt, M., Shindell, D. T., Simpson, I. J., Spahni, R., Steele, L. P., Strode, S. A., Sudo, K., Szopa, S., van der Werf, G. R., Voulgarakis, A., van Weele, M., Weiss, R. F., Williams, J. E., and Zeng, G.: Three decades of global methane sources and sinks, *Nat Geosci*, 6, pp.813-823, 10.1038/NNGEO1955, 2013.
- Lehmann, J. R. K., Münchberger, W., Knoth, C., Blodau, C., Nieberding, F., Prinz, T., Pancotto, V. A., and Kleinebecker, T.: High-Resolution Classification of South Patagonian Peat Bog Microforms Reveals Potential Gaps in Up-Scaled CH₄ Fluxes by use of Unmanned Aerial System (UAS) and CIR Imagery, *Remote Sens-Basel*, 8, article number: 173, 10.3390/rs8030173, 2016.
- 495 Lowry, D., Holmes, C. W., Rata, N. D., O'Brien, P., and Nisbet, E. G.: London methane emissions: Use of diurnal changes in concentration and $\delta^{13}\text{C}$ to identify urban sources and verify inventories, *J Geophys Res-Atmos*, 106, pp.7427-7448, 10.1029/2000jd900601, 2001.
- 500 Nathan, B. J., Golston, L. M., O'Brien, A. S., Ross, K., Harrison, W. A., Tao, L., Lary, D. J., Johnson, D. R., Covington, A. N., Clark, N. N., and Zondlo, M. A.: Near-Field Characterization of Methane Emission Variability from a Compressor Station Using a Model Aircraft, *Environ Sci Technol*, 49, pp.7896-7903, 10.1021/acs.est.5b00705, 2015.
- Nisbet, E., and Weiss, R.: Top-Down Versus Bottom-Up, *Science*, 328, pp.1241-1243, 10.1126/science.1189936, 2010.
- 505 Nisbet, E. G., Manning, M. R., Dlugokencky, E. J., Fisher, R. E., Lowry, D., Michel, S. E., Lund Myhre, C., Platt, M., Allen, G., Bousquet, P., Brownlow, R., Cain, M., France, J. L., Hermansen, O., Hossaini, R., Jones, A. E., Levin, I., Manning, A. C., Myhre, G., Pyle, J. A., Vaughn, B. H., Warwick, N. J., and White, J. W. C.: Very Strong. Atmospheric Methane Growth in the 4 Years 2014-2017: Implications for the Paris Agreement, *Global Biogeochem Cy*, 33, pp.318-342, 10.1029/2018GB006009, 2019.
- 510 O'Shea, S. J., Bauguitte, S. J. B., Gallagher, M. W., Lowry, D., and Percival, C. J.: Development of a cavity-enhanced absorption spectrometer for airborne measurements of CH₄ and CO₂, *Atmos Meas Tech*, 6, pp.1095-1109, 10.5194/amt-6-1095-2013, 2013.



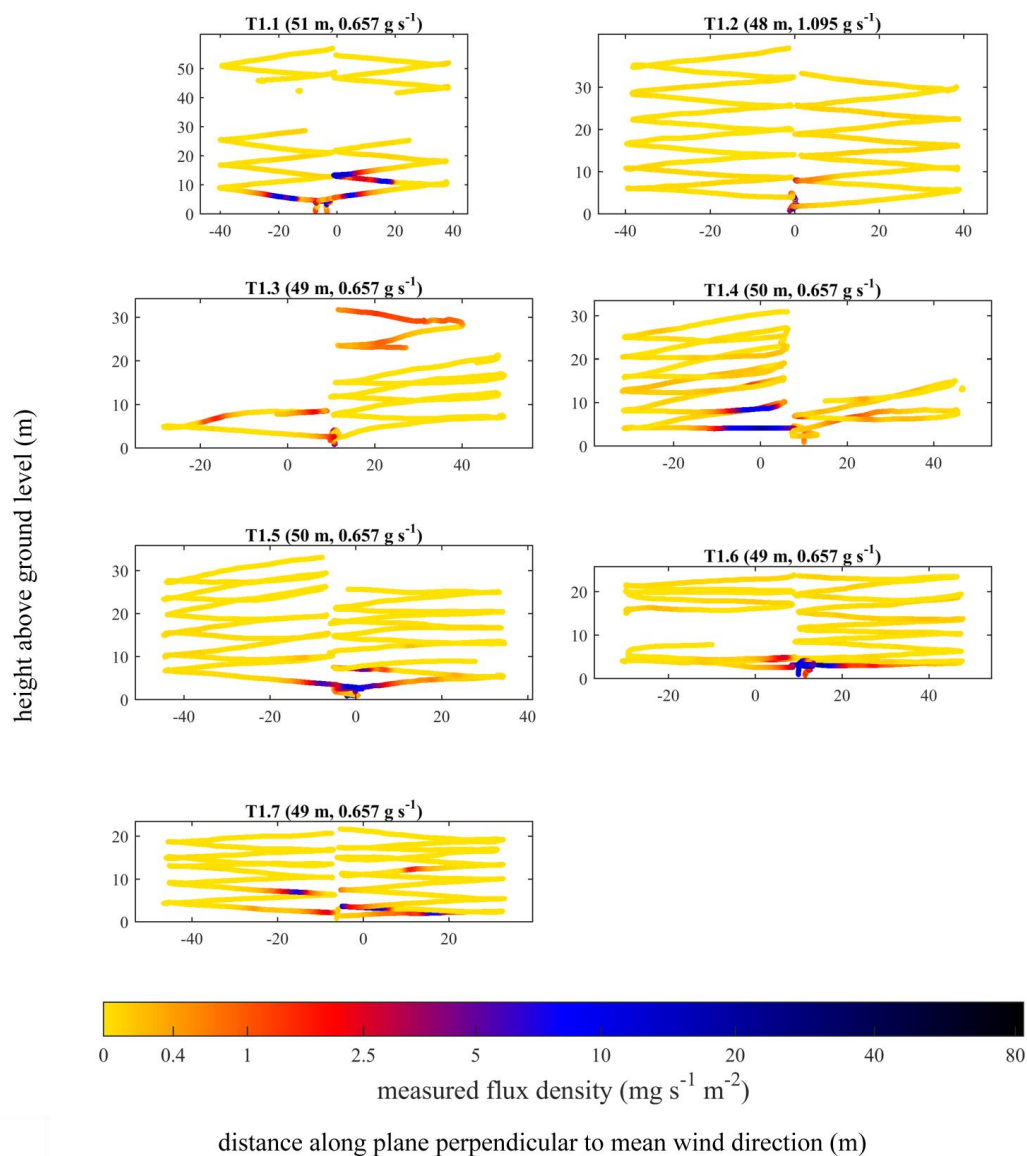
- Paul, J. B., Lapson, L., and Anderson, J. G.: Ultrasensitive absorption spectroscopy with a high-finesse optical cavity and off-axis alignment, *Appl Optics*, 40, pp.4904-4910, 10.1364/Ao.40.004904, 2001.
- 515 Pitt, J. R., Le Breton, M., Allen, G., Percival, C. J., Gallagher, M. W., Bauguitte, S. J. B., O'Shea, S. J., Muller, J. B. A., Zahniser, M. S., Pyle, J., and Palmer, P. I.: The development and evaluation of airborne in situ N₂O and CH₄ sampling using a quantum cascade laser absorption spectrometer (QCLAS), *Atmos Meas Tech*, 9, pp.63-77, 10.5194/amt-9-63-2016, 2016.
- Rella, C. W., Chen, H., Andrews, A. E., Filges, A., Gerbig, C., Hatakka, J., Karion, A., Miles, N. L., Richardson, S. J., Steinbacher, M., Sweeney, C., Wastine, B., and Zellweger, C.: High accuracy measurements of dry mole fractions of carbon dioxide and methane in humid air, *Atmos Meas Tech*, 6, pp.837-860, 10.5194/amt-6-837-2013, 2013.
- 520 Rigby, M., Montzka, S. A., Prinn, R. G., White, J. W. C., Young, D., O'Doherty, S., Lunt, M. F., Ganesan, A. L., Manning, A. J., Simmonds, P. G., Salameh, P. K., Harth, C. M., Muhle, J., Weiss, R. F., Fraser, P. J., Steele, L. P., Krummel, P. B., McCulloch, A., and Park, S.: Role of atmospheric oxidation in recent methane growth, *P Natl Acad Sci USA*, 114, pp.5373-5377, 10.1073/pnas.1616426114, 2017.
- 525 Saunois, M., Bousquet, P., Poulter, B., Peregon, A., Ciais, P., Canadell, J. G., Dlugokencky, E. J., Etiope, G., Bastviken, D., Houweling, S., Janssens-Maenhout, G., Tubiello, F. N., Castaldi, S., Jackson, R. B., Alexe, M., Arora, V. K., Beerling, D. J., Bergamaschi, P., Blake, D. R., Brailsford, G., Brovkin, V., Bruhwiler, L., Crevoisier, C., Crill, P., Covey, K., Curry, C., Frankenberg, C., Gedney, N., Höglund-Isaksson, L., Ishizawa, M., Ito, A., Joos, F., Kim, H. S., Kleinen, T., Krummel, P., Lamarque, J. F., Langenfelds, R., Locatelli, R., Machida, T., Maksyutov, S., McDonald, K. C., Marshall, J., Melton, J. R., Morino, I., Naik, V., O'Doherty, S., Parmentier, F. J. W., Patra, P. K., Peng, C., Peng, S., Peters, G. P., Pison, I., Prigent, C., 530 Prinn, R., Ramonet, M., Riley, W. J., Saito, M., Santini, M., Schroeder, R., Simpson, I. J., Spahni, R., Steele, P., Takizawa, A., Thornton, B. F., Tian, H., Tohjima, Y., Viovy, N., Voulgarakis, A., van Weele, M., van der Werf, G. R., Weiss, R., Wiedinmyer, C., Wilton, D. J., Wiltshire, A., Worthy, D., Wunch, D., Xu, X., Yoshida, Y., Zhang, B., Zhang, Z., and Zhu, Q.: The global methane budget 2000–2012, *Earth Syst Sci Data*, 8, pp.697-751, 10.5194/essd-8-697-2016, 2016a.
- 535 Saunois, M., Jackson, R. B., Bousquet, P., Poulter, B., and Canadell, J. G.: The growing role of methane in anthropogenic climate change, *Environ Res Lett*, 11, article number: 120207, 2016b.
- Scheutz, C., Kjeldsen, P., Bogner, J. E., De Visscher, A., Gebert, J., Hilger, H. A., Huber-Humer, M., and Spokas, K.: Microbial methane oxidation processes and technologies for mitigation of landfill gas emissions, *Waste Manage Res*, 27, pp.409-455, 10.1177/0734242X09339325, 2009.
- 540 Shah, A., Allen, G., Pitt, J. R., Ricketts, H., Williams, P. I., Kabbabe, K., Hollingsworth, P., Helmore, J., Robinson, R., Finlayson, A., Rees-White, T. C., Beaven, R. P., Scheutz, C., and Bourn, M.: A Near-Field Gaussian Plume Inversion Flux Quantification Method, Applied to Unmanned Aerial Vehicle Sampling, *Atmosphere-Basel*, 10, article number: 396, 10.3390/atmos10070396, 2019.
- Villa, T. F., Gonzalez, F., Miljievic, B., Ristovski, Z. D., and Morawska, L.: An Overview of Small Unmanned Aerial Vehicles for Air Quality Measurements: Present Applications and Future Prospectives, *Sensors-Basel*, 16, article number: 1072, 10.3390/S16071072, 2016.
- 545 Wolf, B., Chwala, C., Fersch, B., Garvelmann, J., Junkermann, W., Zeeman, M. J., Angerer, A., Adler, B., Beck, C., Brody, C., Brugger, P., Eméis, S., Dannenmann, M., De Roo, F., Diaz-Pines, E., Haas, E., Hagen, M., Hajsek, I., Jacobeit, J., Jagdhuber, T., Kalthoff, N., Kiese, R., Kunstmann, H., Kosak, O., Krieg, R., Malchow, C., Mauder, M., Merz, R., Notarnicola, C., Philipp, A., Reif, W., Reineke, S., Rödigier, T., Ruehr, N., Schäfer, K., Schrön, M., Senatore, A., Shupe, H., 550 Völksch, I., Wanninger, C., Zacharias, S., and Schmid, H. P.: The SCALEX Campaign Scale-Crossing Land Surface and Boundary Layer Processes in the TERENO-preAlpine Observatory, *B Am Meteorol Soc*, 98, pp.1217-1234, 10.1175/BamsD-15-00277.1, 2017.
- 555 Yang, S. T., Talbot, R. W., Frish, M. B., Golston, L. M., Aubut, N. F., Zondlo, M. A., Gretencord, C., and McSpirt, J.: Natural Gas Fugitive Leak Detection Using an Unmanned Aerial Vehicle: Measurement System Description and Mass Balance Approach, *Atmosphere-Basel*, 9, article number: 383, 10.3390/Atmos9100383, 2018.



560 **Figure 1.** The two fields used for UAV sampling. The map extends 0.71 km horizontally and 0.50 km vertically. The controlled release points are marked by labelled crosses (see Table S3 for details). The background image is taken from ©Google Maps (imagery (2017): DigitalGlobe, GetMapping plc, Infoterra Ltd & Bluesky, The GeoInformation Group).



565 **Figure 2.** [X] measurements acquired by the MGGA and the pMGGA, as a function of sampling duration, for each flight survey, with sampling height above ground level also plotted (coloured dots). A logarithmic colour legend has been used. Vertical blue lines indicate an interruption in continuous sampling.



570

Figure 3. UAV1 flight tracks (coloured dots), with the colour corresponding to q . Periods in which the tubing kinked have been removed. A logarithmic colour legend has been used. The position of the source projected on the plane perpendicular to mean wind direction has been set to a reference of 0 m. The controlled emission flux and the parallel distance of the sampling plane from the source (weighted to the position of q enhancements) are given in brackets.

575

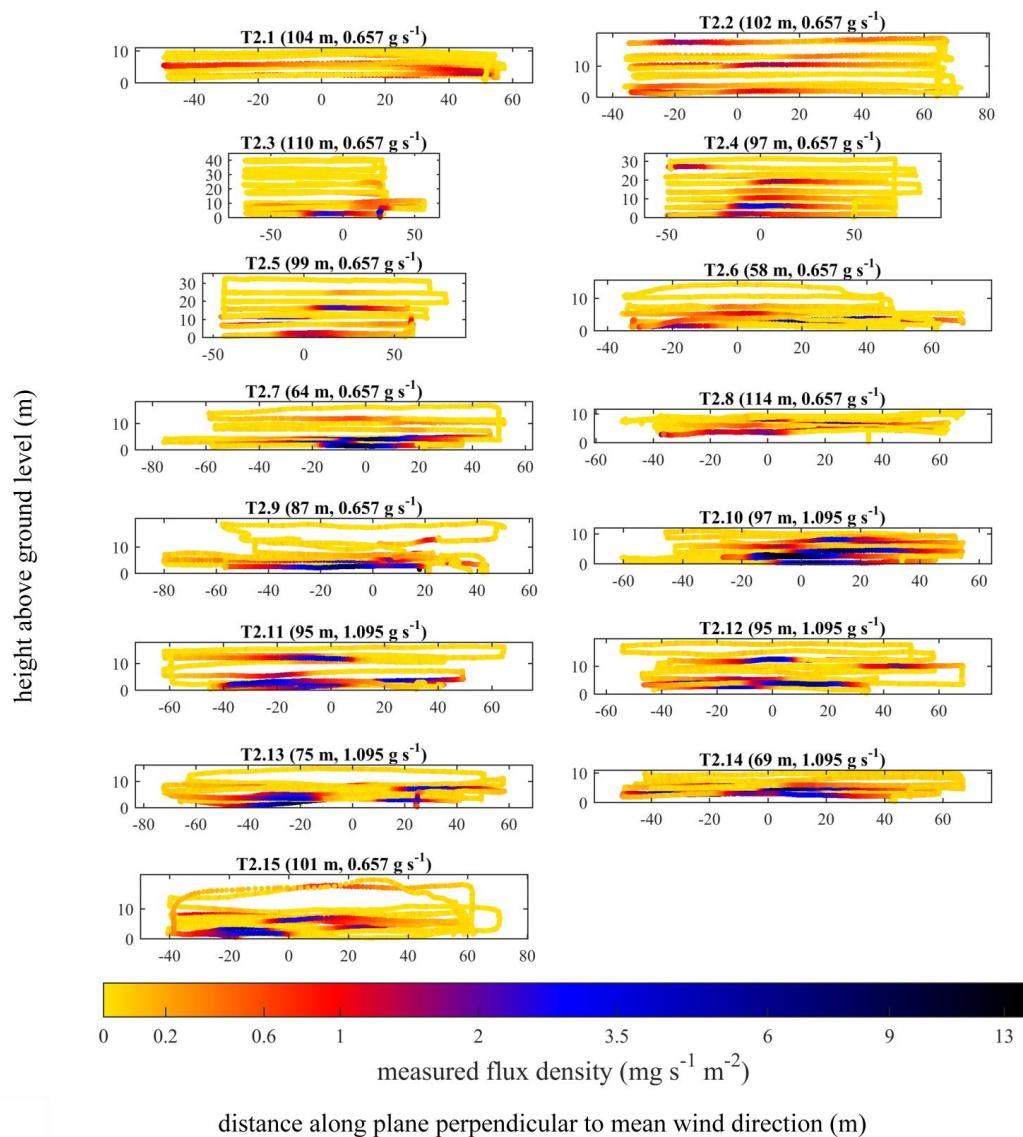
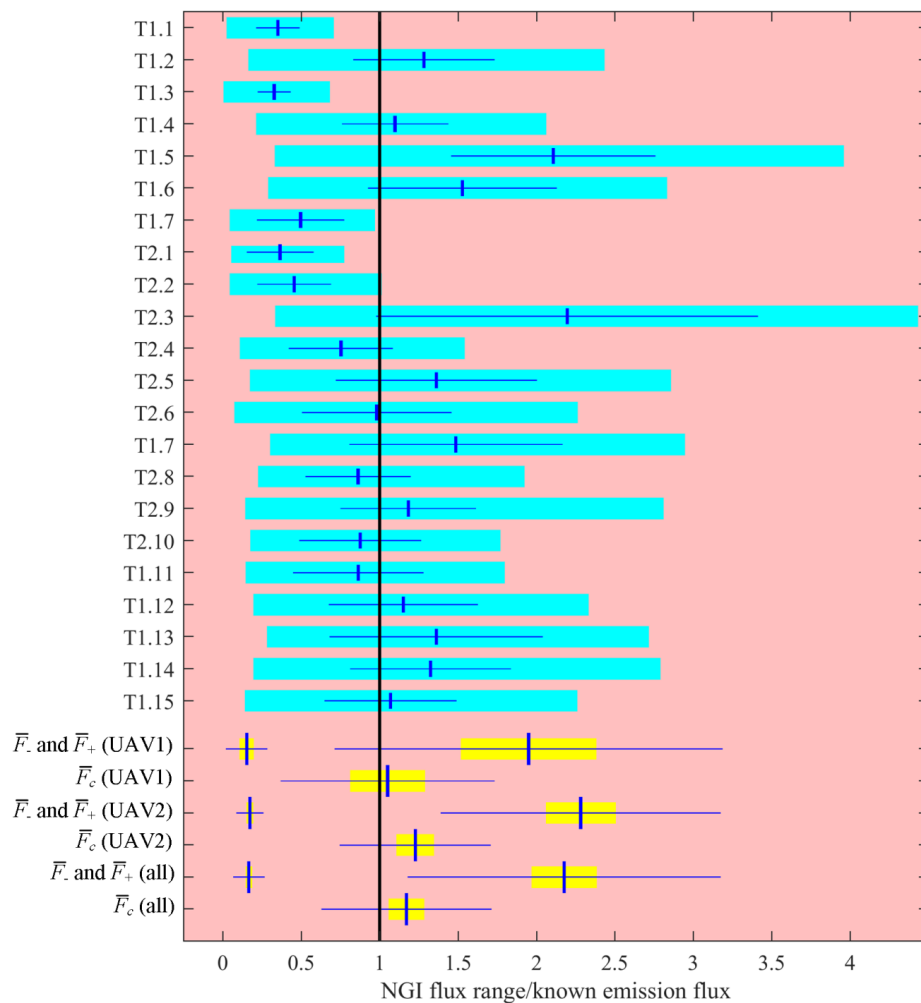


Figure 4. UAV2 flight tracks (coloured dots), with the colour corresponding to q . The position of the source projected on the plane perpendicular to mean wind direction has been set to a reference of 0 m. The controlled emission flux and the parallel distance of the sampling plane from the source (weighted to the position of q enhancements) are given in brackets.

580



585 **Figure 5.** NGI flux uncertainty range (thick cyan bars), for each method testing flight survey, as a fraction of F_0 . The σ_F uncertainty range (horizontal blue lines) is given on either side of F_c (vertical blue lines). \bar{F}_- and \bar{F}_+ averages (vertical blue lines) are plotted for UAV1, UAV2 and for all flight surveys. Standard deviation uncertainty ranges (horizontal blue lines) and standard error uncertainty ranges (thick yellow bars) are given on either side of \bar{F}_- , \bar{F}_+ and \bar{F}_c values.



	MGGA	pMGGA
Mass	4.8 kg	3.4 kg
Length	0.35 m	0.33 m
Width	0.30 m	0.20 m
Depth	0.15 m	0.13 m
Power consumption	35 W	32 W
Operating DC voltage	10 V – 30 V	10 V – 28 V
Cell pressure	atmospheric	pressure controlled to 0.61 bar
E-folding time	(1.6±0.2) s	(3.0±0.1) s
Maximum sampling frequency	10 Hz	5 Hz
σ_{AV}	2.71 ppb	5.44 ppb
1 Hz Allan deviation	0.71 ppb	2.2 ppb
0.1 Hz Allan deviation	0.24 ppb	0.72 ppb
Optimum integration time	(20±3) s	(70±10) s

Table 1: General properties of the MGGA and the pMGGA.

590



	MGGA	pMGGA
<i>a</i>	-0.00557	-0.000503
<i>b</i>	+0.00530	+0.000704
<i>w</i>	23.6 ppm	23.6 ppm
<i>α</i>	-1.556	-1.640
<i>β</i>	-12.25	-1.208
σ_v	0.0004253	0.0002613

Table 2: Water correction coefficients for the MGGA and pMGGA, required to obtain v using Eq. (4).



	MGGA	pMGGA
$G \pm \sigma_G$	0.9970 \pm 0.00023	0.9869 \pm 0.00028
$C \pm \sigma_C$	(+0.0132 \pm 0.0020) ppm	(-0.0019 \pm 0.0015) ppm

Table 3: Calibration coefficients for the MGGA and pMGGA.



	UAV1	UAV2
Flights per survey	2	1
Distance of sampling plane from source	48 m – 51 m	64 m – 104 m
Take-off and landing	Manual	Manual
Flight control	Waypoints	Manual (course lock)
Average velocity across the sampling plane	$(1.5 \pm 0.1) \text{ m s}^{-1}$	$(2.8 \pm 0.6) \text{ m s}^{-1}$
Payload	PFA tubing and inlet, wind sensor	pMGGA
Height of plane of propellers	0.540 m	0.680 m
Height of air inlet	0.845 m	0.370 m

595 Table 4: A comparison between UAV1 and UAV2.